



Zeng, Z., Zhou, M., Esmaily, M., Zhu, Y., Choudhary, S., Griffith, J., & Et, AL. (2022). Corrosion resistant and high-strength dual-phase Mg-Li-Al-Zn alloy by friction stir processing. *Communications Materials*, 3(1), [18]. <https://doi.org/10.1038/s43246-022-00245-3>

Publisher's PDF, also known as Version of record

License (if available):
CC BY

Link to published version (if available):
[10.1038/s43246-022-00245-3](https://doi.org/10.1038/s43246-022-00245-3)

[Link to publication record in Explore Bristol Research](#)
PDF-document

This is the final published version of the article (version of record). It first appeared online via Springer Nature at <https://doi.org/10.1038/s43246-022-00245-3>. Please refer to any applicable terms of use of the publisher

University of Bristol - Explore Bristol Research

General rights

This document is made available in accordance with publisher policies. Please cite only the published version using the reference above. Full terms of use are available: <http://www.bristol.ac.uk/red/research-policy/pure/user-guides/ebr-terms/>

Corrosion resistant and high-strength dual-phase Mg-Li-Al-Zn alloy by friction stir processing

Zhuoran Zeng¹✉, Mengran Zhou^{2,3,4,5}✉, Marco Esmaily^{6,7,8}, Yuman Zhu^{6,9}, Sanjay Choudhary⁶, James C. Griffith^{6,10,11}, Jisheng Ma^{6,10}, Yvonne Hora^{10,12}, Yu Chen¹³, Alessio Gullino^{6,14}, Qingyu Shi^{2,3,4}, Hidetoshi Fujii⁵ & Nick Birbilis¹

Magnesium is the lightest structural metal, and alloying with lithium makes it even lighter. However, multi-phase Mg-Li alloys typically undergo rapid corrosion, and their strength decreases at room temperature due to natural age-softening. Here, we engineer a rapidly degrading dual-phase Mg-Li-Al alloy to be durable via friction stir processing followed by liquid CO₂ quenching. The best performing alloy has a low electrochemical degradation rate of 0.72 mg·cm⁻²·day⁻¹, and high specific strength of 209 kN·m·kg⁻¹. We attribute this electrochemical and mechanical durability to its microstructure, which consists of a refined grain size of approximately 2 μm and dense nanoprecipitates. This microstructure suppressed the formation of the detrimental AlLi phase, and an aluminium-rich protective surface layer also formed. This processing route might be useful for designing lightweight and durable engineering alloys.

¹ College of Engineering and Computer Science, Australian National University, Canberra, ACT 2601, Australia. ² Department of Mechanical Engineering, Tsinghua University, 100084 Beijing, China. ³ State Key Laboratory of Tribology, Department of Mechanical Engineering, Tsinghua University, 100084 Beijing, China. ⁴ Key Laboratory for Advanced Materials Processing Technology, Department of Mechanical Engineering, Tsinghua University, 100084 Beijing, China. ⁵ Joining and Welding Research Institute (JWRI), Osaka University, Osaka 565-0871, Japan. ⁶ Department of Materials Science and Engineering, Monash University, Clayton, VIC 3800, Australia. ⁷ Department of Materials Science and Engineering, Massachusetts Institute of Technology, Cambridge, MA 02139, USA. ⁸ Volvo Materials Technology Laboratory, Volvo Group, Lundby, Gothenburg 417 15, Sweden. ⁹ Monash Centre for Additive Manufacturing, Monash University, Clayton, VIC 3800, Australia. ¹⁰ Monash X-ray Platform, Monash University, Clayton, VIC 3800, Australia. ¹¹ Bristol Composites Institute, CAME School of Engineering, University of Bristol, Bristol BS8 1TR, UK. ¹² Department of Chemical and Biological Engineering, Monash University, Clayton, VIC 3800, Australia. ¹³ Monash Centre of Electron Microscopy, Monash University, Clayton, VIC 3800, Australia. ¹⁴ Department of Applied Science and Technology, Politecnico di Torino, Torino 10129, Italy. ✉email: zhuoran.zeng@anu.edu.au; zhoumr888@mail.tsinghua.edu.cn

Magnesium (Mg) has the lowest density (1.74 g cm^{-3}) of the engineering metals, ~65% the density of aluminium alloys and 25% that of steel. The high specific strength of Mg alloys makes them attractive materials for the demands of lightweighting in transport and consumer electronics¹. However, poor formability and rapid degradation of Mg and its alloys have significantly limited their wider industrial adoption². One effective way to tackle the formability issue is to add adequate lithium (Li) into Mg alloys. This is because a ductile body-centred cubic (BCC) β -phase will form in the hexagonal close-packed (HCP) matrix α -phase when the alloyed Li concentration is over ~5 wt. % (full β -phase structure will present for a Li concentration > ~10.3 wt. %)^{3,4}. The induction of β -phase in Mg–Li alloy system has brought significant advantages over other Li-free Mg alloys. Firstly, the major lithium addition can further reduce the alloy density to the level of ~1.3 g cm^{-3} , the lightest among all Mg alloys. Secondly, the appearance of the β -phase can overcome the limited deformation modes of α -Mg at room temperature and significantly improve formability. The ductility of β -phase-containing Mg–Li alloy can exceed 50% tensile elongation at room temperature, whilst most ductile Mg–Zn–RE/Ca alloys have elongation less than 40%⁵. Such benefits stimulated rapid development of Mg–Li alloys for defence and aerospace industries in the US^{6,7} and the former Soviet Union^{8,9}, since firstly patented in 1935¹⁰. In the 1960s, NASA researchers optimised and applied ultra-lightweight LA141 (Mg–14Li–1.5Al), whilst researchers in the Soviet Union developed MA18 (Mg–11Li–0.9Al–2.2Zn–0.1Mn–0.2Ce) and MA21 (Mg–8Li–5Al–1.5Zn–4.5Cd–0.3Mn–0.1Ce) alloys^{8,9}.

Despite vastly improved formability, the strength of Mg–Li alloys is very low, typically as low as about 100 MPa, due to the existence of a soft β phase. One approach to enhance the alloy strength is to add additional alloying elements. With the addition of Al, the Mg–Li–Al-containing β -phase can be strengthened after water quenching from high temperatures, and the resultant yield strength can be increased to >400 MPa^{11–13}. Such a unique quench strengthening in Mg–Li–Al alloy has been attributed to the formation of a supersaturated solid solution and MgAlLi₂ θ precipitates in early studies^{14–17}, and nano-sized Al-rich zones and Mg₃Al D0₃ nano-precipitates during rapid cooling in recent reports^{12,13}. Given the low density of alloy, the specific property of quenched-strengthened Mg–Li–Al alloy is enormous and better than other Mg alloys including high-strength Mg–RE alloys¹². However, the adverse effect along with the water-quench treatment is the brittleness of the Al-alloyed β -phase. Prior studies have already demonstrated that full BCC–Mg–Li–Al alloys after water quenching had nearly no plasticity^{11,12,18}, making it almost not usable. To obtain reasonable ductility, Li and Al concentration has to be decreased so that the alloy has $\alpha + \beta$ dual-phases³. Typically, the ductility increased from nearly zero to ~18% after the concentration of Li and Al decreased from 13 and 5% to and 3% (all in wt.%), respectively¹⁸.

For $\alpha + \beta$ dual-phases Mg–Li–Al alloys, however, the major issue is their rapid corrosion^{19–21}. The β phase (BCC Mg–Li) has an even lower standard potential than the α -phase (HCP Mg–Li)²², establishing a localised corrosion morphology that arises from microgalvanic coupling within the microstructure, where the β -phase is the local anode site. Consequently, the mass-loss rate of $\alpha + \beta$ dual-phase Mg–Li alloys is about 4–6 times more than that of the popular commercial Mg alloy AZ31 in marine atmospheres²³, which is not acceptable for most applications. Micro-galvanic coupling is an inherent problem for dual-phase Mg–Li alloys, and how to achieve a high corrosion resistance for such alloys remains unclear.

In addition to poor electrochemical durability, the quench-strengthened Mg–Li–Al alloys are not mechanically durable. The strength of the quenched alloy was found to decrease rapidly at room temperature^{14–17}. It was reported that the ultimate tensile

strength of quenched Mg–11Li–1Al–0.5Zn alloy dropped from 226 MPa to ~155 MPa within 1000 h at room temperature¹⁷. The hardness of water-quenched Mg–11Li–3Al alloy was decreased by ~40 HV in 1 year¹³. The natural age-softening occurs because the metastable Mg₃Al or MgAlLi₂ θ precipitates tend to coarsen and transform to a stable but soft AlLi phase, even at room temperature^{12–17}. This issue has greatly limited the adoption of Mg–Li alloys for industrial applications where a stable property profile is a prerequisite. Although considerable efforts have been made since 1940s, the electrochemical and mechanical durability of Mg–Li alloy is still not satisfactory. With these unresolved issues, research interest and efforts in Mg–Li alloys have been dwindling since 1970s³, despite increasingly strong demand for ultra-lightweight alloys, and whilst Mg–Li alloys are still the lightest structural alloys.

In this work, it is demonstrated that the issues of alloy durability that have been puzzling this research field for more than 70 years—may be solved. Herein, a model alloy of dual-phase Mg–9Li–4Al–1Zn (LAZ941) with a density of 1.47 g cm^{-3} was used. This alloy has low strength and rapid corrosion rate in the as-rolled state, and a rapid age-softening following annealing and water quenching (WQ). To enhance the alloy properties, the alloy microstructure was deliberately engineered by developing a novel thermomechanical process that consists of friction stir processing, immediately followed by liquid CO₂ quenching (denoted as FSP hereafter). The FSP was capable of substantially refining the grain size. Liquid CO₂ provides a greater cooling rate than water; thus the grains and precipitates formed during quenching are finer, from less time at a high temperature which stifles grain growth and precipitate coarsening. Not only did the strength and ductility of the Mg–Li alloy following FSP exceed such properties possible from WQ, but mechanical and electrochemical durability were also substantially enhanced. The alloy presented has the lowest degradation rate among all Mg alloys reported previously, with minor softening from natural ageing within 2 years. The purpose of this paper was to report this phenomenon and discuss the underlying mechanism for exceptional mechanical and electrochemical durability.

Results

Electrochemical durability. FSP substantially improved the electrochemical durability of LAZ941. After 48 h of immersion in 0.1 M NaCl, the hydrogen evolution rate of the FSP sample was low, at about $0.1 \text{ ml cm}^{-2} \text{ day}^{-1}$ and the mass-loss rate was $0.72 \text{ mg cm}^{-2} \text{ day}^{-1}$. In contrast, the as-rolled sample showed a significantly higher corrosion rate (Supplementary Fig. 1). The hydrogen evolution rate and mass-loss rate were $0.55 \text{ ml cm}^{-2} \text{ day}^{-1}$ and $1.86 \text{ mg cm}^{-2} \text{ day}^{-1}$, respectively.

The electrochemical durability was further assessed using potentiodynamic polarisation and electrochemical impedance spectroscopy (EIS) methods. Prior to commencing polarisation testing, open-circuit potential (OCP) was stabilised for 1 h (Fig. 1a), revealing that the FSP sample exhibited a more ‘noble’ OCP than the as-rolled sample. The polarisation curves in Fig. 1b showed a reduced corrosion current density in the FSP sample ($2.8 \mu\text{A cm}^{-2}$), ~10 times lower than that of the as-rolled sample ($\sim 32 \mu\text{A cm}^{-2}$). In the EIS test, the FSP sample showed a much lower dissolution kinetic than the as-rolled sample (Fig. 1c). However, it is noted that without liquid CO₂ quenched, the air-cooled LAZ941 after FSP demonstrated similar corrosion resistance to the as-rolled LAZ941 in the electrochemical testing, but much worse than that of FSP-LAZ941 with liquid CO₂ quenching. The results suggest that it is liquid CO₂ quenching after FSP, rather FSP itself, resulted in the enhanced electrochemical durability.

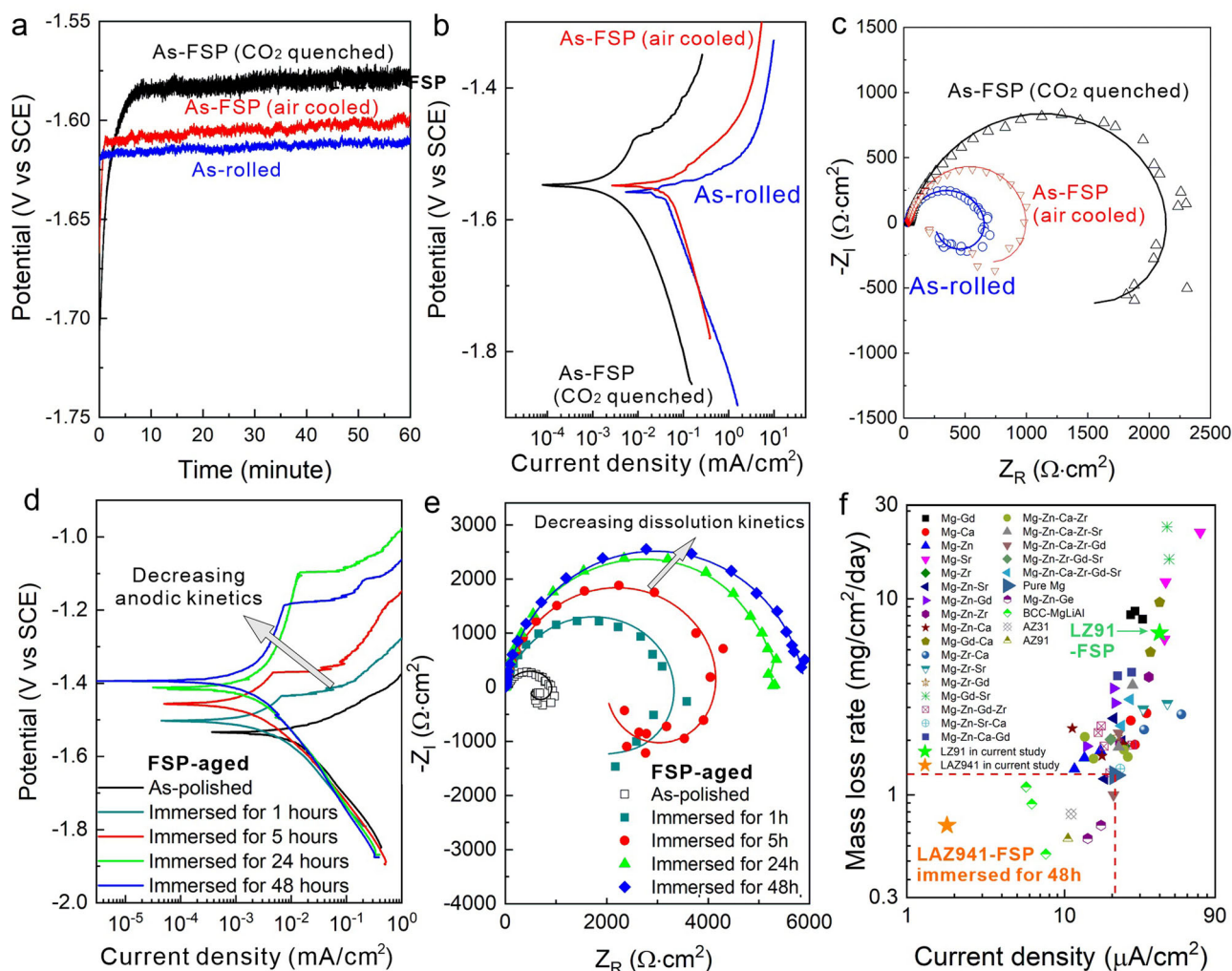


Fig. 1 Measurement of electrochemical durability. Electrochemical tests showing (a) open-circuit potential, (b) potentiodynamic polarisation curves, and (c) EIS Nyquist plots of as-rolled and as-FSP-samples after 1-h immersion in 0.1 M NaCl solution. d, e potentiodynamic polarisation and EIS results of FSP-aged samples (FSP and CO₂ quenched followed by naturally-aged for 2 years) during immersion. f Comparison of mass-loss rate and corrosion current density of FSP-LAZ941 alloy with some typical Mg alloys^{11,24–26}, including Mg-11Li-3Al alloy¹¹, and corrosion-resistant Mg-Zn-Ge alloys²⁴. Red dashed lines in (f) showing the mass-loss rate and corrosion current density of pure Mg²⁵ as a benchmark.

Following natural ageing for 2 years, the FSP-aged sample in the as-polished state (Fig. 1d) retained corrosion resistance similar to the as-FSP sample (Fig. 1b). During the immersion in NaCl electrolyte, the anodic kinetic decreased with the increase of immersion time and finally stabilised at 1.6–1.8 $\mu\text{A cm}^{-2}$. The EIS results also showed that dissolution kinetics decreased with the increased exposure time—which is concomitant to the temporal evolution of a protective surface film upon the alloy (Fig. 1e). The experimental results demonstrated that dual-phase Mg–Li–Al alloy can have significant corrosion resistance relative to all Mg alloys to date (Fig. 1f)^{11,24–26}, including those already identified as corrosion-resistant, such as BCC–Mg–Li alloy¹¹ and Mg alloys with dilute germanium addition²⁴.

The corroded surface was characterised by different techniques to reveal the mechanism of the outstanding corrosion resistance. Profilometry (Fig. 2a, b) showed that the FSP-aged sample had a ‘smoother’ surface following immersion in 0.1 NaCl for 48 h. Its surface roughness was typically within $\pm 1 \mu\text{m}$, with some deviations in the range of several microns associated with discrete surface features. In contrast, the as-rolled sample had a ‘rougher’ surface—which was also impacted by localised corrosion manifestation with localised corrosion sites with depths of

many tens of microns. The scanning electron microscopy (SEM) observation of the sample cross-section supported the profilometer results (Fig. 2c–f). The FSP-aged sample had a uniform and intact surface after immersion, without any visible localised corrosion penetrating into bulk (Fig. 2c). The energy dispersive X-ray spectrum (SEM-EDXS) mapping showed uniform oxygen distribution on the sample surface (Fig. 2d). In contrast, in the as-rolled sample, the dissolution and cracking of corrosion product into the bulk by more than 100 μm (Fig. 2e), with oxygen localised at the corrosion sites (Fig. 2f). Such localised corrosion was initiated in the β -phase (Supplementary Fig. 2a, b). As a comparison, for the FSP-aged sample, although some surface dissolution was uniformly distributed in both α - and β -phases at the early stage of immersion testing, there was no localisation of dissolution after 48 h of immersion (Supplementary Fig. 2c–j). The intact surface observed from different view directions suggests the formation of a protective layer that covers both α - and β -phases after the sample was processed by FSP. The higher oxygen concentration in the EDXS map (Fig. 2d) further suggested an oxygen-rich layer on the FSP sample after immersion; the surface layer also appeared to have a higher Al concentration.

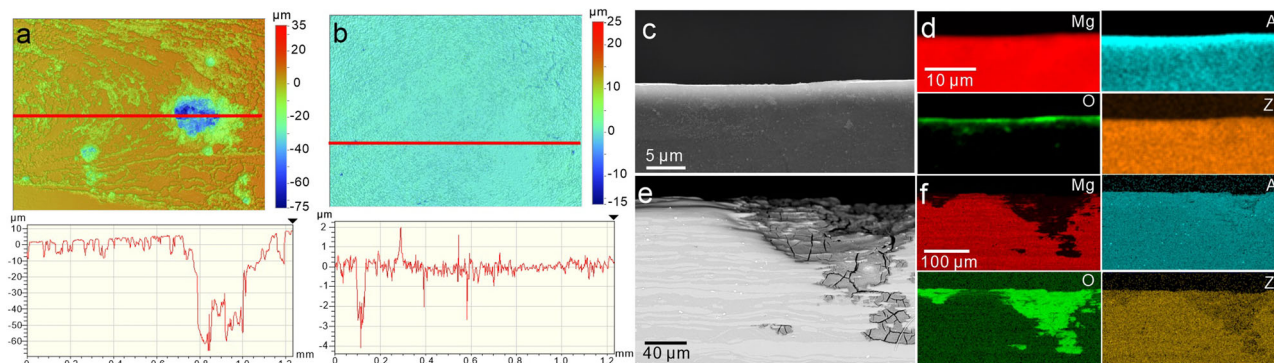


Fig. 2 Surface observation of as-rolled and FSP-aged samples after immersion in 0.1M NaCl solution for 48 h. **a, b** Profilometer observation of corroded surface of **(a)** as-rolled and **(b)** FSP-aged sample and **(c–f)** SEM images and corresponding EDS mapping of cross-section showing surface roughness of **(c, d)** FSP-aged and **(e, f)** as-rolled samples.

The surface layer structure of FSP-aged sample was further characterised at higher magnification using scanning transmission electron microscopy (STEM) EDXS for the lamellae prepared by focused ion beam (FIB) lift-out (Supplementary Fig. 3). It was found that the oxygen-rich layer on the FSP sample (500–1000 nm in thickness) contained numerous $\text{Mg}(\text{OH})_2$ flakes (Supplementary Fig. 3a, b). Between the flakes and bulk, there was a thin (~ 50 nm) and dense layer with a higher concentration of Al (Supplementary Fig. 3c). Selected area diffraction of surface layer showed the diffraction pattern of MgO and Al_2O_3 (Supplementary Fig. 4). The increased concentration of Al was also captured by X-ray photoelectron spectroscopy (XPS) and grazing incident X-ray diffraction (GIXRD). From the XPS survey spectra, the percentage atomic concentration of Al on the surface was 5.3% in the FSP-aged sample and 2.4% in the as-rolled sample (Supplementary Fig. 5a). A qualitative assessment of the increased amount of Al in the FSP-aged sample compared to the as-rolled sample can also be made from the $\text{Al}2p$ region scans (Supplementary Fig. 5b). The distinct symmetrical peak in the FSP sample at ~ 74 eV with no shoulder/peak at ~ 72 eV (metal) is indicative that Al was predominantly in the form of Al_2O_3 or $\text{Al}(\text{OH})_3$. GIXRD scan profile showed $\text{Al}(\text{OH})_3$ peak in the FSP sample, but not in the as-rolled sample, when they both were immersed under the same condition (Supplementary Fig. 6a, b).

Mechanical durability. In addition to electrochemical durability, mechanical properties and durability were also be substantially enhanced via FSP. Figure 3a showed that the yield strength of the WQ-LAZ941 sample increased to 260 MPa—which was similar to that of the previously reported BCC Mg–11Li–3Al alloy¹¹. However, both WQ samples had low ductility ($\sim 4\%$ for LAZ941 and $\sim 1.5\%$ for WQ–Mg–11Li–3Al). In comparison, the FSP-LAZ941 alloy had an enhanced yield strength of 308 MPa and a ductility of 16.5%. More critically, the high-strength state of FSP-LAZ941 was almost stable (Fig. 3b). After a slight decrease in hardness from 109 to 98 HV within 3 months, any further reduction in hardness was marginal. Throughout nearly 2 years of natural ageing, the hardness of the FSP sample decreased by less than 15%. In contrast, the hardness of the WQ sample demonstrated a rapid and significant decrease. The alloy hardness dropped by more than 45 HV (40%) within the first 3 months. To further demonstrate the stability of the property profile, the alloy strength was measured following natural ageing by tensile testing. It was determined that the yield strengths of the FSP sample were 303 MPa and 274 MPa after 1 week and 3 months, respectively (Fig. 3c). Following 12 months, the yield strength was still high (268 MPa). This value was still much higher than the yield strength of as-FSP-LAZ941, when it was air-cooled and no liquid

CO_2 quenching is applied. The yield strength of air-cooled FSP-LAZ941 was 193 MPa with high ductility of 35% (Fig. 3c). In contrast, after natural ageing for 6 months, the yield strength of WQ sample decreased to 141 MPa, a similar value to that of the as-rolled sample. Tensile test results were consistent with the hardness measurement. Considering the low density of LAZ941 alloy, the as-FSP and FSP-aged samples had a high specific yield strength ($182\text{--}209$ kN m kg⁻¹). In Fig. 3d, the specific yield strength and elongation of WQ-, FSP- and FSP-aged LAZ941 samples are compared with other Mg alloys⁵ including recently reported high-strength Mg–Li–Al alloy^{11,12}, high-strength AlCuLi 2195-T8 alloy², and other FSP–Mg alloys^{27–40}, and FSP–Al alloys^{41–45}. Although the FSP-LAZ941 is not the one with the highest specific yield strength, its specific yield strength is higher than the majority of Mg alloys, including those processed by FSP. More importantly, the FSP-LAZ941 also had significant tensile ductility, and such high specific strength–ductility synergy has not been commonly observed in Mg alloys due to the typical strength–ductility trade-off. Following natural ageing, the FSP-LAZ941 continues to present exceptional specific strength and an even more outstanding strength–ductility balance.

Microstructural examination. To investigate the origin of the enhanced electrochemical and mechanical durability, the microstructure of as-rolled, WQ-, and FSP-samples were examined in the as-processed state and during natural ageing. The as-rolled sample had large and elongated grains (Fig. 4a) and a high density of spherical AlLi particles in the β -phase (Fig. 4b). The averaged diameter of particles was measured ~ 0.41 μm (Supplementary Fig. 7a, b). These particles contained a higher concentration of Al and Zn (Supplementary Fig. 7c–e). The high oxygen concentration of AlLi particle indicated that it was oxidised when the sample was exposed to open air (Supplementary Fig. 6f). In the as-WQ condition, the AlLi particles disappeared, but they were observed again after natural ageing for 1 year (Fig. 4c, d). In contrast, after FSP sample was natural-aged for 2 years, the AlLi particles were still not observed (Fig. 4e, f).

To validate the SEM surface observation, X-ray diffraction (XRD) was used to reveal the evolution of AlLi during thermomechanical processing and natural ageing in bulk. Local spectra with 2θ between 22° and 25° are resampled to highlight peaks from (111) MgLiAl_2 θ -phase (22.97°) and (111) AlLi phase ($2\theta = 24.37^\circ$), but excluded the peaks from α and β matrix. The high peak of AlLi phase in XRD pattern supported that the spherical particles observed in the as-rolled condition (Fig. 4b) were AlLi phase. Upon heating, AlLi phase started to dissolve above 300°C (Fig. 4g). Given that the temperature induced by FSP was measured as $\sim 430^\circ\text{C}$ (Supplementary Fig. 8), the AlLi

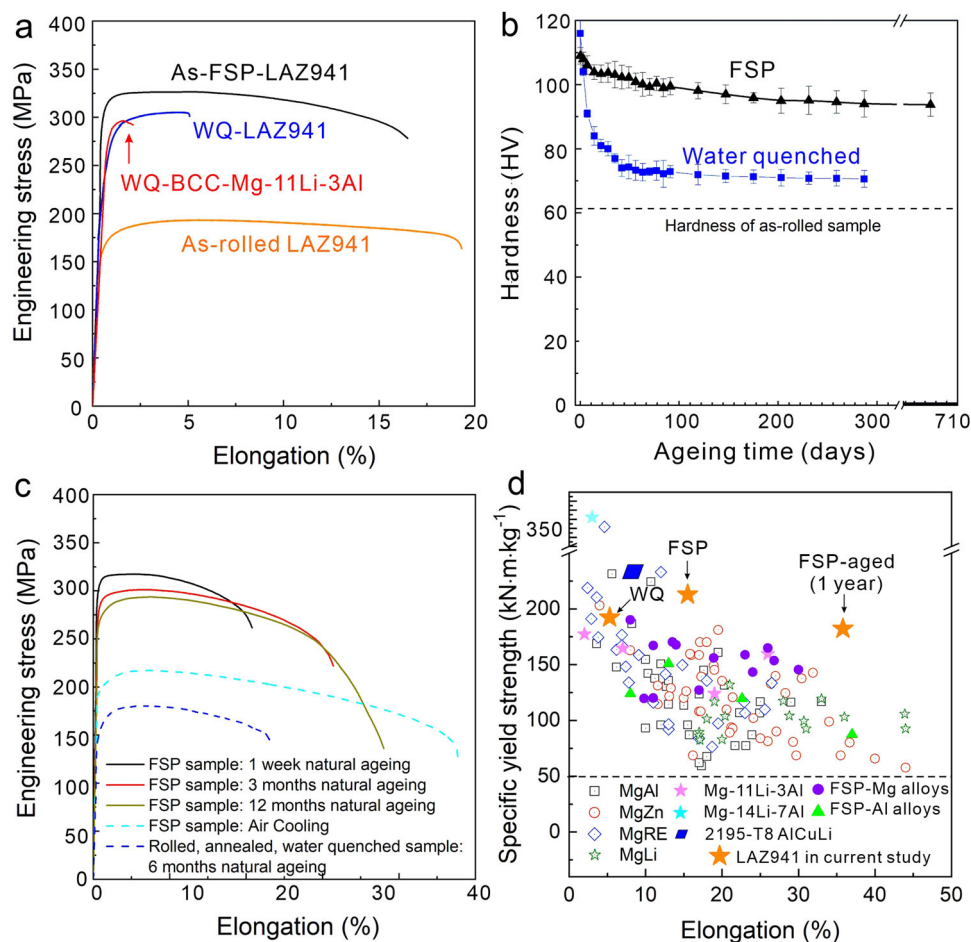


Fig. 3 Mechanical properties. **a** Tensile stress–strain curves of LAZ941 alloy in the as-rolled, FSP and WQ states in contrast to that of WQ-Mg-11Li-3Al benchmark. **b** Hardness of WQ- and FSP-LAZ941 samples during natural ageing up to 2 years. **c** Tensile stress–strain curves of FSP-LAZ941 alloy after natural ageing for 1 week, 3 and 12 months, in contrast to that of as-FSP-LAZ941 (air-cooled and no liquid CO₂ applied) and WQ-LAZ941 alloy after natural ageing for 6 months. **d** Comparison of specific yield strength and elongation of WQ- and FSP-LAZ941 alloy with other Mg alloys, high-strength AlCuLi alloy, FSP-Mg and FSP-Al alloys in tensile test^{2,5,11,12,27–45}.

particles were expected to be dissolved during FSP, as the phase diagram (Supplementary Fig. 9a) shows AlLi should dissolve at 320 °C. In the as-WQ and as-FSP conditions, the diffraction peaks of AlLi phase were not detected (Fig. 4h). Instead, the diffraction peak of the metastable θ phase appeared in the as-WQ sample. Following 1-year natural ageing, the AlLi peak was observed, which is consistent with SEM observations. Different from the WQ sample, in the as-FSP sample, neither θ nor AlLi peaks were observed (Fig. 4i). Even after natural ageing up to 2 years, the AlLi peak did not appear; instead, the θ phase presented and was the only intermetallic phase. Full spectra of XRD results is provided in Supplementary Fig. 10. From the full spectra, the D0₃-Mg₃Al peak at 2θ of 37° (shown by red arrow in Supplementary Fig. 10c) as reported in ref. 13, is not observable. Therefore, the XRD results support the intermetallics in FSP and FSP-aged samples are θ phase rather than Mg₃Al phase.

While the SEM and XRD did not reveal any intermetallic phase in the as-FSP state, a high density of nano-precipitates (~5 nm in diameter) was observed inside the β -phase of an as-FSP sample (Fig. 5a–c). The high-angle annular dark-field (HAADF) STEM images showed that the crystal lattice of the precipitates was almost the same as that of the surrounding matrix (Fig. 5b, c). The inset fast-Fourier transformation (FFT) pattern in Fig. 5c revealed characteristic diffractions from these precipitates, which is consistent with a previous report for the θ phase (L₂₁ ordered

structure)¹⁶. From the FFT, the lattice parameter a is measured of 6.72 ± 0.02 Å, which is closer to the a_{θ} (6.7 Å)¹⁶, but different to the $a_{\text{Mg}_3\text{Al}}$ (6.8 Å)¹³. Following natural ageing for 3 months, the precipitates seemed to coarsen and exhibit a plate shape (Fig. 5d). They were about 100–200 nm in length and ~10 nm in thickness, and had a high concentration of Al (Fig. 5e). After natural ageing for 2 years, the θ precipitates were even thickened (Fig. 5f, g). Under this circumstance, the spherical AlLi particles were not observed, consistent with SEM and XRD results.

Discussion

In this work, FSP was coupled with immediate CO₂ quenching to specifically engineer microstructure to deliver outstanding durability (i.e. durability not previously realised in this or in other Mg-alloy systems). As a severe plastic deformation technique, it is well-established that FSP can significantly refine grain size⁴⁶. However, highly dispersed and coherent nano-precipitates, which is uncommon in Mg alloys, have been observed here for the first time in the Mg–Li-based alloy. In other systems, such as Al alloys⁴⁷, steels⁴⁸, and high entropy alloys⁴⁹, nano-clusters and coherent nano-precipitates have been observed and reported to be the key for strengthening alloys without sacrificing ductility. Such strengthening effects originate from heterogeneous solute distribution as higher stress is required for dislocations to cut through the clusters/coherent precipitates⁴⁸, which is also posited

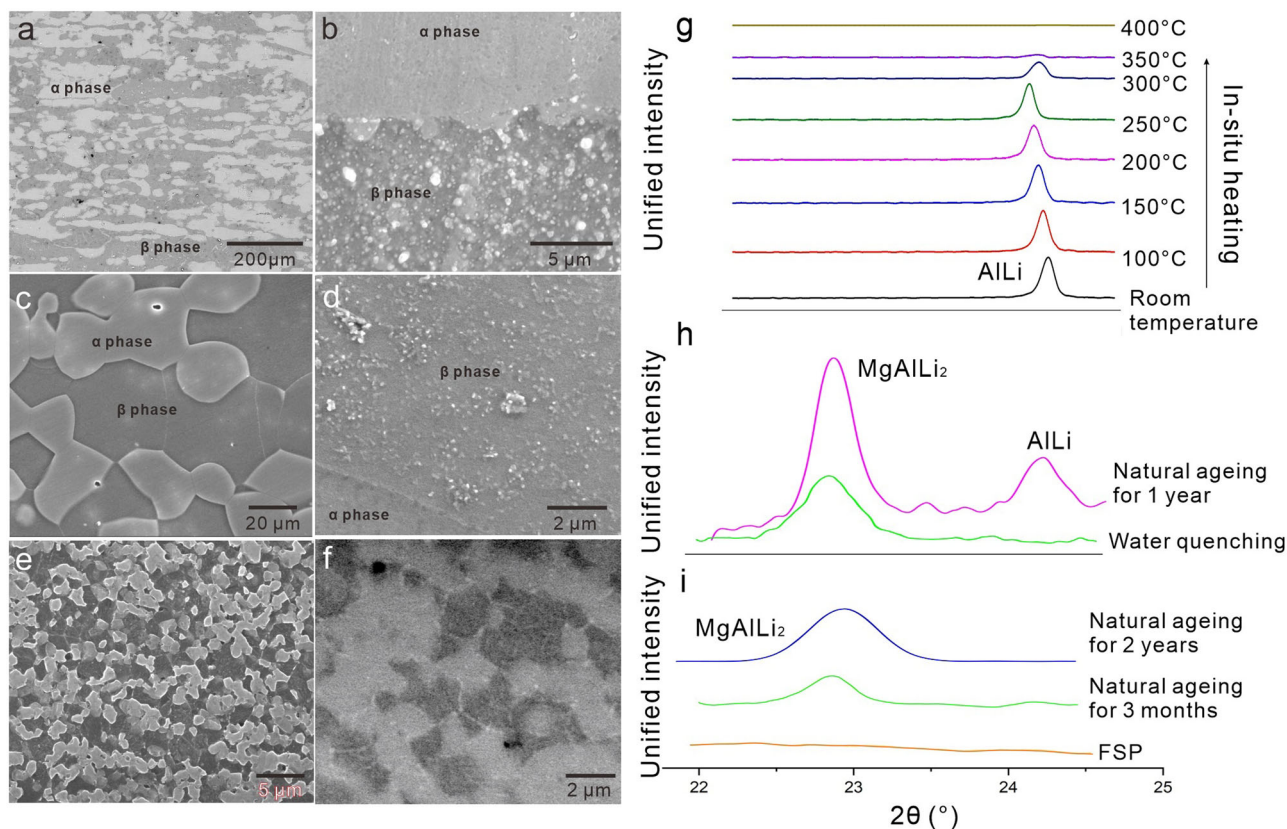


Fig. 4 SEM and XRD characterisation of microstructure evolution in natural ageing. **a–f** SEM images of samples at the states of **(a, b)** as-rolled, **(c)** WQ, **(d)** WQ-aged for 1 year, **(e)** FSP and **(f)** FSP-aged for 2 years. **g–i** XRD θ - 2θ scan between 22° and 25° showing the AlLi (111) peak and MgAlLi₂ (111) peak during **(g)** in situ heating, **(h)** WQ and natural ageing for 1 year, and **(i)** FSP and natural ageing up to 2 years.

as the mechanism for the precipitate strengthening of FSP-LAZ941 in this study.

Whilst nano-clusters/precipitates in Al alloys and steels were induced by ageing or cyclic loading for a long-treatment time, the nano-precipitates formed in LAZ941 alloy are likely to result from the rapid CO₂ quenching process. Equilibrium CALPHAD simulation (using Pandat[®]) has shown that the solubility of Al above 325 °C is 2.9 wt.% and 4.1 wt.% in α - and β -phase of LAZ941 alloy, respectively, but it will decrease to nearly zero at room temperature (Supplementary Fig. 9b–d). Although the CALPHAD simulation is independent to the various processing histories and microstructures presented, the simulation results demonstrate that (i) the temperature during FSP is sufficiently high to dissolve AlLi particles, and (ii) the solubility of Al in both α and β phases at room temperature is very low so that the driving force to form precipitates from supersaturated solid solution is high. When the cooling rate is slow, such as air cooling (1.7 °C/s, Supplementary Fig. 8), there is sufficient time for Al atoms to diffuse so that the precipitate can reach an equilibrium state at high temperatures (Supplementary Fig. 11). With a more rapid cooling rate, such as water quench (~200 °C/s), semi-coherent precipitates form between 140 and 170 °C¹³, due to insufficient time for precipitate coarsening and transformation. Then, it is reasonable to speculate that if the cooling rate is fast enough, the duration at elevated temperature is so short that it only allows clustering of supersaturated Al solute atoms to form an ordered structure that is coherent to the matrix. It was measured that liquid CO₂ quench only took 0.6 s for the sample from 360 to 100 °C during FSP, shorter than 1.4 s via water quench.

The unique microstructure consisting of uniformly refined grains and nano-precipitates is posited to not only result in

strengthening but also be the origin of the enhanced mechanical durability. The high density of grain boundaries and α/β phase boundaries induced by FSP, were posited to delay the precipitation coarsening and suppress the transformation to equilibrium AlLi phase. As observed in Supplementary Fig. 12, these boundaries provide a reservoir of Al atoms that otherwise would possibly contribute to precipitate coarsening and transformation. The Al atoms are expected to segregate to the grain boundaries or α/β phase boundaries, because these sites have more significant lattice distortion, as demonstrated in Supplementary Fig. 13. In contrast, nano-precipitates seem to have coherent interphase with the matrix. According to the Lifshitz–Slyozov–Wagner theory^{50,51}, the decrease in the lattice mismatch between precipitate and matrix, and thus the reduction of interface energy, would suppress the particle coarsening. In the WQ sample, grain size is ~10 times larger than that of FSP sample ($2.3 \pm 0.8 \mu\text{m}$ in diameter). Consequently, the Al atoms in the matrix are less likely to segregate to grain boundaries in the WQ sample, but remaining in the matrix facilitating precipitate coarsening and transforming to large and equilibrium AlLi particles. For the WQ sample, the strengthening is predominantly caused by the formation of θ phase during quenching, whilst strengthening from other factors such as grain refinement, is marginal. Once the majority of θ phase is coarsened and transformed into spherical AlLi phase, the intermetallic phase can no longer provide sufficient strengthening, and the alloy strength decreases back to that similar of as-rolled state. As a comparison, in the FSP-aged sample, although the θ phase is coarsened, it still has a high density and is not transformed to equilibrium AlLi phase. Moreover, different from WQ, FSP significantly refined grain size, and grain refinement is expected to contribute significant

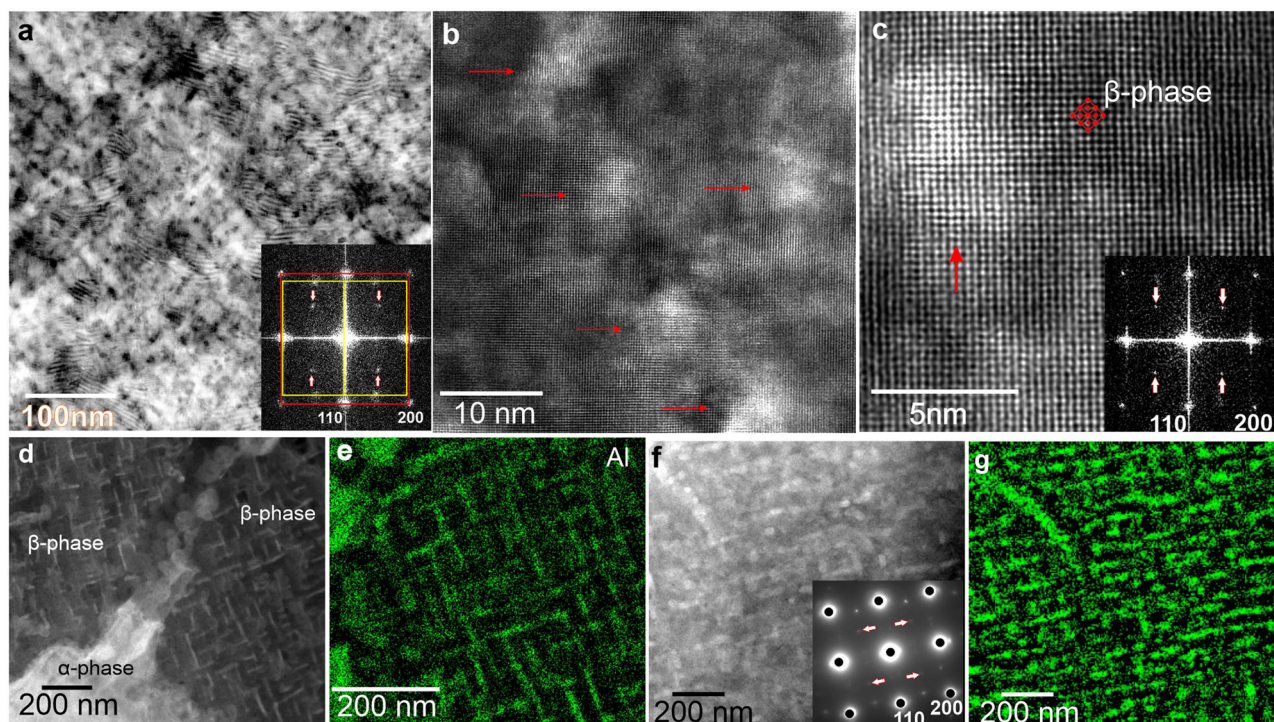


Fig. 5 TEM characterisation of the evolution of intermetallic phases in FSP sample during natural ageing. **a** BF-STEM showing dense nano-precipitates and **(b, c)** atomic-scale HAADF-STEM showing the structure of nano-precipitates in the β -phase matrix, as indicated by red arrows. **d–g** HAADF-STEM images and corresponding EDS-STEM Al mapping of FSP sample after natural ageing for **(d, e)** 3 months and **(f, g)** 2 years. Yellow and red frames in the inset FFT pattern in **(a)** indicated the diffractions from the α and β phase, and arrows in inset FFT in **(a, c)** and diffraction pattern in **(f)** indicated the diffraction from the θ phase. The incident beam was parallel to $[001]_{\beta}$.

strengthening. Even when θ nano precipitates are coarsened during natural ageing, the refined grains are still capable of providing considerable strengthening, and thus the decrease in strength and hardness is not significant.

The suppression of phase transformation to equilibrium AlLi phase from supersaturated Al solution with nano- θ -precipitates also contributes to electrochemical durability, namely, lower rates of alloy corrosion. Although the enhancement of corrosion resistance by supersaturated Al in the Mg matrix and fine particles was reported in Mg–Al binary alloy, it should be noted that the $Mg_{17}Al_{12}$ particle is nobler than Mg matrix⁵². In contrast, the relative potential of AlLi phase (300–400 mV more negative than β -phase⁵³) notionally stimulates localised corrosion by AlLi serving as an anode in micro-galvanic coupling. Once AlLi particles are dissolved, the prevalence of localised corrosion diminishes, however a tendency for micro-galvanic coupling between α - and β -phases can still exist. Thus the high corrosion resistance in the FSP sample still needs further justification—although it is understood that the uniformity of composition across the FSP sample plays a key role. In previous studies, outstanding corrosion resistance was reported in BCC Mg–Li alloys, due to the dynamic evolution of a Li_2CO_3 surface film^{11,20,54–56}. This mechanism for the dual-phase Mg–Li alloys has not been previously observed, because at the more macro-scale, Li_2CO_3 surface film was suggested to form principally on β -phase (which has a higher Li concentration) rather than the α -phase^{11,57}. As the signal of Al element was detected on immersed FSP sample by different techniques (Supplementary Figs. 3–6), it is posited speculated that a complex Al-containing film, as an alternative to a principally Li_2CO_3 surface film, is the key to the corrosion resistance in the dual-phase LAZ941 alloy. In other words, the presence of Al is deemed a critical facet to the high corrosion resistance of FSP-LAZ941. To validate this postulate, the FSP-

LAZ941 alloy was compared with a Mg–9Li–1Zn (LZ91) that is Al-free, in corrosion tests. Although both alloys were absent of AlLi particles, the mass-loss and hydrogen evolution rate of LZ91 alloy were substantially higher (Supplementary Fig. 1). The electrochemical tests showed that corrosion current density of LZ91 is $95 \mu A cm^{-2}$ in the as-rolled condition and $40 \mu A cm^{-2}$ after FSP (Supplementary Fig. 14a), ten times more than that of LAZ941 alloy after FSP. The EIS data also revealed increased dissolution kinetics for LZ91, compared with FSP LAZ941 (Supplementary Fig. 14b). The corrosion resistance of LZ91-FSP sample is much worse than many of Mg alloys (Fig. 1f).

In previous studies regarding Mg alloys, such as Mg–Y–RE⁵⁸, a considerable increase in corrosion resistance was observed due to grain refinement. The refinement of microstructure may accelerate the formation of surface films and reduce the micro-galvanic reaction, which can lead to more uniform and shallow corrosion morphology. Whilst significant grain refinement is also induced by FSP in this study, grain refinement itself is unlikely to result in such a substantial increase in electrochemical durability of dual-phase Mg–Li-based alloy. Otherwise, the FSP-LZ91 and FSP-LAZ941 (air-cooled) should show much enhanced corrosion resistance, but in fact, FSP-LZ91 and FSP-LAZ941 (air-cooled) only showed similar mass loss and hydrogen evolution rate to the as-rolled counterpart samples (Fig. 1a–c and Supplementary Fig. 1). These test results support the notion that Al solute, rather than merely microstructure refinement, played a critical role in surface protection in the corrosive environment. To further support this claim, a fresh surface of FSP-LAZ941 sample was prepared and exposed to open air for two hours, before GIXRD and XPS depth profiling was performed. The peak for Al_2O_3 , despite weak, was observed in the GIXRD pattern (Supplementary Fig. 15a). Supplementary Fig. 15b shows elemental distribution along the depth profiling. In the surface and near-surface XPS

scans, a distinct symmetrical peak at higher binding energy overshadowed much smaller metallic peaks at lower binding energies, indicating Al was predominantly in the form of Al_2O_3 or $\text{Al}(\text{OH})_3$ here. At ~ 90 nm the metallic peaks became more pronounced with a corresponding decrease in oxide/hydroxide peak intensity, a trend that continued with depth to ~ 200 nm. Deconvoluting the oxide/hydroxide and metallic regions of the Al2p spectra at each depth indicates a changing composition with depth (Supplementary Fig. 15c). No Li_2CO_3 peak was detected by GIXRD. The XPS depth profile also showed zero Li concentration from the surface to 90 nm depth (Supplementary Fig. 15b). The metallic elements from 0–90 nm were predominantly Mg and Al, with an Al/Mg ratio of ~ 0.23 at the surface decreasing to ~ 0.14 at a depth of 246 nm (Supplementary Fig. 15d). The high Al/Mg ratio suggests that the participation of Al in a complex oxide/carbonate was deemed important.

Conclusion. Herein, it was demonstrated that exceptional stability of alloy property profile, including simultaneous electrochemical and mechanical durability, could be achieved via microstructural engineering. The key to realising such properties for an Mg–Li–Al alloy was to achieve fine grain size and a high density of coherent nano-precipitates. This could be achieved by thermomechanical processing followed by rapid cooling. Under such fabrication circumstances, the formation of the coarse equilibrium AlLi phase will be suppressed. It is envisaged that the findings here provide a new strategy for designing and developing durable products for various industries.

Methods

Materials preparation. Hot-rolled Mg–9Li–4Al–1Zn wt.% (LAZ941) plates were provided by AMLi Material Technology Co. Ltd., and hot-rolled Mg–9Li–1Zn benchmark plates were provided by Xi'an Sifang Ultralight Material Co. Ltd. The rolled plates for FSP had a length of 200 mm, a width of 70 mm, and a thickness of 2.5 mm. FSW was performed with a cemented tungsten carbide (WC) tool. The tool had a shoulder diameter of 15 mm, a probe diameter of 6 mm, and a probe length of 2.4 mm. The tool travel direction was parallel to the sheet rolling direction. It was then friction stir processed at the WC tool rotation speed of 600 rpm. Liquid CO_2 (-78.5°C) was utilised to ensure rapid cooling so that the grain coarsening was suppressed. The setup is illustrated in Supplementary Fig. 16.

Mechanical testing. Dog-bone-shaped samples for tensile testing were prepared using an electrical discharge machine (EDM, Sodick AG360L). Test specimens had a gauge length of 5 mm, and were parallel to the tool's travel direction. The tensile test was performed in an Instron 4505 mechanical test machine with a crosshead speed of 0.3 mm/min. Three samples were tested per processing condition.

Electrochemical and immersion testing. Electrochemical measurements were performed with a three-electrodes flat cell (K-0235, Princeton Applied Research) with a Saturated Calomel Electrode (SCE) as the reference, and platinum mesh as the counter electrode. Test specimens (working electrode) were mounted in epoxy resin, followed by grinding to a 2000 grit finish using SiC paper under ethanol. All the electrochemical tests were carried out by using 200 ml of 0.1 M NaCl. A Bio-Logic[®] VSP potentiostat was utilised for all electrochemical testing.

Potentiodynamic polarisation measurements were obtained following open-circuit potential (OCP) conditioning for 1 h, where an overpotential of ± 0.3 V vs OCP was applied, using a scan rate of 1 mV/s. The Tafel-type fitting and determination of corrosion current density and corrosion potential were obtained by EC-lab[®] Software (version 11.27).

Electrochemical impedance spectroscopy (EIS) was performed over the frequency range of 100 kHz to 10 mHz, with a polarising signal of 10 mV. All tests were carried out at least in triplicates. The obtained spectra were fit using EC-lab[®] software (version 11.27). EIS result obtained after fitting the results using equation $|Z| = R_s + \frac{1}{j\omega C_{dl} + \frac{1}{R_{ct} + \frac{1}{R_L + j\omega L}}}$, where R_s , R_{ct} and R_L represent the solution resistance, the charge transfer resistance and resistance associated with the inductive loop. ω is the angular frequency, and C_{dl} is the capacitance of the electric double layer.

For immersion testing, samples were immersed in a 200 ml of quiescent 0.1 M NaCl for 20 and 48 h, at room temperature (maintained at 23°C). Prior to immersion, the samples were ground to 4000 grit, then mirror polished with colloidal silica solution, sonicated in ethanol, air-dried and weighted with a calibrated balance with an accuracy of 0.01 mg. In order to combine the mass-loss

experiment with the volumetric hydrogen collection in a single step, an inverted funnel was placed over the immersed sample and the evolved hydrogen was collected inside a burette. Before removing the corrosion products with a solution of 20% CrO_3 for 15 s, the corrosion morphology was characterised using scanning electron microscopy. After removing the corrosion products and assessing the mass loss, optical profilometry (OP) was carried out using a Veeco Wyko NT1100 in vertical scanning interferometry (VSI) mode. The OP analysis was carried out in three different zones upon each sample covering an area of 1.2 mm by 0.9 mm for each measurement.

X-ray diffraction. X-ray diffraction (XRD) and in situ XRD heating and cooling were performed using a Bruker D8 Advance X-ray diffractometer using Cu-K α radiation ($\lambda = 0.154$ nm) operating at 40 kV and 40 mA, with step size 0.01° from 20° to 80° in 2θ angle. The X-ray diffraction data were processed using TOPAS 4.2 software. The XRD was calibrated using the National Institute of Standards and Technology standard reference material LaB $_6$. The sample for in situ XRD was under nitrogen atmosphere protection. GIXRD with an incident angle of 0.6° was performed in a high-resolution PANalytical X'Pert PRO MRD system using Cu-K α radiation operating at 45 kV and 40 mA.

Scanning electron microscopy and transmission electron microscopy. Scanning electron microscopy (SEM), using an FEI Quanta 3D FEG and Zeiss Ultra-Plus, along with transmission electron microscopy (TEM) using an FEI Tecnai F20 FEG and FEI Titan³ 80–300; were used for microstructural characterisation. Atomic resolution scanning TEM (STEM) images were obtained from a double-corrected FEI Titan³ 80–300 operating at 300 kV with a collection inner semi-angle of 40 mrad. The convergence angle was set to 15.0 mrad, leading to a probe diameter of ~ 0.12 nm. The samples for SEM characterisation are prepared by 4000 SiC sandpaper grinding, and 50 nm colloidal silica suspension polishing. Specimens for TEM characterisation were 3 mm diameter discs prepared by spark cutting, followed by mechanical grinding to a thickness of 50 μm using 4000 grid SiC paper. Samples were then ion-polished using a Gatan Precision Ion Polishing System (voltage 4.8 kV and angle 4°) at -100°C , until a small hole formed in the specimen.

Following immersion for 48 h in 0.1 M NaCl solution, electron transparent cross-section lamellae were extracted from specimen surfaces (to inspect surface/corrosion films) using a Zeiss Crossbeam system. For preparing the lamellae, a thin layer of Pt was deposited on the area of interest to protect the surface film before sectioning with a focused Ga ion beam. The sectioned lamellae were subsequently welded to Cu grids using Pt deposition through micromanipulation. Fine polishing was applied using Ga ion to remove redeposit and potentially FIB damaged layer and the final thickness of lamellae was reduced to approximately 100 nm. JOEL2100 is used for the TEM and STEM-EDS characterisation of the lift-out lamellae.

X-ray photoelectron spectroscopy. X-ray photoelectron spectroscopy (XPS) was performed using a Thermo Scientific Nexsa Surface Analysis System calibrated to Au 4f and equipped with a hemispherical analyser. The incident radiation was monochromatic Al K α X-rays (1486.6 eV) at 72 W (6 mA and 12 kV, $400 \times 800 \mu\text{m}^2$ spot). Survey (wide) and high-resolution (narrow) scans were recorded at analyser pass energies of 150 eV and 50 eV and step sizes of 1.0 eV and 0.1 eV, respectively. The base pressure in the analysis chamber was less than 5.0×10^{-9} mbar. A low-energy dual-beam (ion and electron) flood gun was used to compensate for surface charging. For the depth profile, sputtering was carried out using a monatomic Ar⁺ gas cluster ion source at 4000 eV and high current. Each level was sputtered with a 2-mm raster size, rotation and a 5 s delay. Data processing was carried out using Avantage software version 5.9921 and the energy calibration was referenced to the main line of C1s at 284.8 eV.

Data availability

The authors declare that the main data supporting the findings of this study are available within the article and its Supplementary Information files. Extra data are available from the corresponding author upon request.

Received: 11 August 2021; Accepted: 21 March 2022;

Published online: 06 April 2022

References

- Pollock, T. M. Weight loss with magnesium alloys. *Science* **328**, 986–987 (2010).
- Polmear, I., StJohn, D., Nie, J. F. & Qian, M. *Light Alloys*, Fifth Edition. (Butterworth-Heinemann, 2017).
- Cain, T. W. & Labukas, J. P. The development of β phase Mg–Li alloys for ultralight corrosion resistant applications. *npj Mater. Degrad.* **4**, 17 (2020).
- Wu, R. et al. Recent progress in magnesium–lithium alloys. *Int. Mater. Rev.* **60**, 65–100 (2015).

5. Zeng, Z. R., Stanford, N., Davies, C. H. J., Nie, J. F. & Birbilis, N. Magnesium extrusion alloys: a review of developments and prospects. *Int. Mater. Rev.* **64**, 1–36 (2018).
6. Bryer, T. G., Frost, P. D. & White, E. L. *Final Technical Report on the Development of Magnesium-Lithium Alloys for Structural Applications. Report to National Aeronautics and Space Administration. Contract NAS8-5049* (Battelle Memorial Institute, 1963).
7. Jackson, R. J. & Frost, P. D. *Properties and Current Applications of Magnesium-Lithium Alloys*. NASA SP-5068 (1967).
8. Koryagin, Y. D. On the structural state stability of superlight MA21 magnesium-lithium alloy. *Izv Vyssh Uchebn Zaved, Tsvetn Metall.* **14**, 94–97 (1982).
9. Elkin, F. M. & Davydov, V. G. Russian ultralight constructional Mg–Li alloys: their structure, properties, manufacturing, applications. in *Magnesium Proceedings of the 6th International Conference Magnesium Alloys and Their Applications* (ed. Kainer, K. U.) 94–99 <https://doi.org/10.1002/3527603565.ch13> (2003).
10. Brown, R. H. & Willey, L. A. Magnesium duplex metal. *United States patent 2*, 011,613 (1935).
11. Xu, W. et al. A high-specific-strength and corrosion-resistant magnesium alloy. *Nat. Mater.* **14**, 1229–1235 (2015).
12. Xin, T. et al. Ultrahigh specific strength in a magnesium alloy strengthened by spinodal decomposition. *Sci. Adv.* **7**, 3039 (2021).
13. Tang, S. et al. Precipitation strengthening in an ultralight magnesium alloy. *Nat. Commun.* **10**, 1003 (2019).
14. Busk, R. S., Leman, D. L. & Casey, J. J. The properties of some magnesium-lithium alloys containing aluminum and zinc. *JOM* **2**, 945–951 (1950).
15. Frost, P. D., Kura, J. G. & Eastwood, L. W. Aging characteristics of magnesium-lithium base alloys. *JOM* **2**, 1277–1282 (1950).
16. Alamo, A. & Banchik, A. D. Precipitation phenomena in the Mg-31 at% Li-1 at% Al alloy. *J. Mater. Sci.* **15**, 222–229 (1980).
17. Matsuzawa, K., Koshihara, T., Ochiai, S. & Kojima, Y. The effect of additional element on the age-hardening characteristics and properties of Mg-Li alloys. *J. Japan. Inst. Light. Metal.* **40**, 659–665 (1990).
18. Hsu, C. C., Wang, J. Y. & Lee, S. Room temperature aging characteristic of MgLiAlZn alloy. *Mater. Trans.* **49**, 2728–2731 (2008).
19. Polmear, I. Grades and alloys. in *ASM Specialty Handbook: Magnesium and Magnesium Alloys* (eds Avedesian, M. A. & Baker, H.) 19–20 (ASM International, 1999).
20. Li, C. Q. et al. Composition and microstructure dependent corrosion behaviour of Mg-Li alloys. *Electrochim. Acta* **260**, 55–64 (2018).
21. Dobkowska, A., Adamczyk-Cieslak, B., Mizera, J., Kubásek, J. & Vojtěch, D. Corrosion behaviour of magnesium lithium alloys in NaCl solution. *Solid State Phenom.* **227**, 87–90 (2015).
22. Esmaily, M. et al. Fundamentals and advances in magnesium alloy corrosion. *Prog. Mater. Sci.* **89**, 92–193 (2017).
23. Frost, P. D., Fink, F. W., Pray, H. A. & Jackson, J. H. Results of some marine-atmosphere corrosion tests on magnesium-lithium alloys. *J. Electrochem. Soc.* **102**, 215 (1955).
24. Liu, R. L., Zeng, Z. R., Scully, J. R., Williams, G. & Birbilis, N. Simultaneously improving the corrosion resistance and strength of magnesium via low levels of Zn and Ge additions. *Corros. Sci.* **140**, 18–29 (2018).
25. Xia, X. *The Effect of Composition on the Electrochemical Properties and Corrosion of Wrought Mg-alloys*. Thesis, Monash University. (2015).
26. Kateryna, G., Davies, C. H. J., Scully, J. R. & Birbilis, N. Corrosion of magnesium alloys: the role of alloying. *Int. Mater. Rev.* **60**, 169–194 (2014).
27. Huang, Y., Li, J., Wan, L., Meng, X. & Xie, Y. Strengthening and toughening mechanisms of CNTs/Mg-6Zn composites via friction stir processing. *Mater. Sci. Eng. A* **732**, 205–211 (2018).
28. Dinaharan, I., Zhang, S., Chen, G. & Shi, Q. Development of titanium particulate reinforced AZ31 magnesium matrix composites via friction stir processing. *J. Alloy. Compd.* **820**, 153071 (2020).
29. Liang, J. et al. Fabrication and mechanical properties of CNTs/Mg composites prepared by combining friction stir processing and ultrasonic assisted extrusion. *J. Alloy. Compd.* **728**, 282–288 (2017).
30. Khan, M. D. F., Karthik, G. M., Panigrahi, S. K. & Janaki Ram, G. D. Friction stir processing of QE22 magnesium alloy to achieve ultrafine-grained microstructure with enhanced room temperature ductility and texture weakening. *Mater. Charact.* **147**, 365–378 (2019).
31. Freney, T. A. & Mishra, R. S. Effect of friction stir processing on microstructure and mechanical properties of a cast-magnesium–rare earth alloy. *Metall. Mater. Trans. A* **41**, 73 (2009).
32. Yang, Q., Xiao, B. & Ma, Z. Influence of process parameters on microstructure and mechanical properties of friction-stir-processed Mg-Gd-Y-Zr casting. *Metall. Mater. Trans. A* **43**, 2094–2109 (2012).
33. Huang, Y. et al. Dynamic recrystallization and mechanical properties of friction stir processed Mg-Zn-Y-Zr alloys. *J. Mater. Process. Tech.* **249**, 331–338 (2017).
34. Jamili, A. M., Zarei-Hanzaki, A., Abedi, H. R., Minárik, P. & Soltani, R. The microstructure, texture, and room temperature mechanical properties of friction stir processed Mg-Y-Nd alloy. *Mater. Sci. Eng. A* **690**, 244–253 (2017).
35. Zheng, F. Y. et al. Microstructures and mechanical properties of friction stir processed Mg–2.0Nd–0.3Zn–1.0Zr magnesium alloy. *J. Magnesium Alloy.* **1**, 122–127 (2013).
36. Yang, C. W. Effect of friction stir processing on the microstructural evolution and tensile behaviors of an α/β Dual-phase Mg-Li-Al-Zn Alloy. *Mater. Trans.* **55**, 371–377 (2014).
37. Kumar, N., Dendge, N., Banerjee, R. & Mishra, R. S. Effect of microstructure on the uniaxial tensile deformation behavior of Mg-4Y-3RE alloy. *Mater. Sci. Eng. A* **590**, 116–131 (2014).
38. Kumar, N., Choudhuri, D., Banerjee, R. & Mishra, R. S. Strength and ductility optimization of Mg–Y–Nd–Zr alloy by microstructural design. *Int. J. Plasticity* **68**, 77–97 (2015).
39. Cao, G., Zhang, D., Luo, X., Zhang, W. & Zhang, W. Effect of aging treatment on mechanical properties and fracture behavior of friction stir processed Mg–Y–Nd alloy. *J. Mater. Sci.* **51**, 7571–7584 (2016).
40. Long, F., Chen, G., Zhou, M., Shi, Q. & Liu, Q. Simultaneous enhancement of mechanical properties and corrosion resistance of as-cast Mg-5Zn via microstructural modification by friction stir processing. *J. Magnesium Alloy.* <https://doi.org/10.1016/j.jma.2021.08.029> (2021).
41. Nakata, K., Kim, Y. G., Fujii, H., Tsumura, T. & Komazaki, T. Improvement of mechanical properties of aluminum die casting alloy by multi-pass friction stir processing. *Mater. Sci. Eng. A* **437**, 274–280 (2006).
42. Liu, Z. Y., Xiao, B. L., Wang, W. G. & Ma, Z. Y. Analysis of carbon nanotube shortening and composite strengthening in carbon nanotube/aluminum composites fabricated by multi-pass friction stir processing. *Carbon* **69**, 264–274 (2014).
43. Ke, L., Huang, C., Xing, L. & Huang, K. Al–Ni intermetallic composites produced in situ by friction stir processing. *J. Alloy. Compd.* **503**, 494–499 (2010).
44. Chen, Y. et al. Influence of multi-pass friction stir processing on the microstructure and mechanical properties of Al-5083 alloy. *Mater. Sci. Eng. A* **650**, 281–289 (2016).
45. El-Rayes, M. M. & El-Danaf, E. A. The influence of multi-pass friction stir processing on the microstructural and mechanical properties of aluminum alloy 6082. *J. Mater. Process. Tech.* **212**, 1157–1168 (2012).
46. Ma, Z. Y. Friction stir processing technology: a review. *Metall. Mater. Trans. A* **39**, 642–658 (2008).
47. Sun, W. W. et al. Precipitation strengthening of aluminum alloys by room-temperature cyclic plasticity. *Science* **363**, 972–975 (2019).
48. Jiang, S. et al. Ultrastrong steel via minimal lattice misfit and high-density nanoprecipitation. *Nature* **544**, 460–464 (2017).
49. Fu, Z. et al. A high-entropy alloy with hierarchical nanoprecipitates and ultrahigh strength. *Sci. Adv.* **4**, 8712 (2018).
50. Lifshitz, I. M. & Slyozov, V. V. The kinetics of precipitation from supersaturated solid solutions. *J. Phys. Chem. Solids* **19**, 35–50 (1961).
51. Wagner, C. Theorie der alterung von niederschlägen durch umlösen (Ostwald-reifung). *Zeitschrift für Elektrochemie* **65**, 581–591 (1961).
52. Wu, P. P., Song, G. L., Zhu, Y. X., Feng, Z. L. & Zheng, D. J. The corrosion of Al-supersaturated Mg matrix and the galvanic effect of secondary phase nanoparticles. *Corros. Sci.* **184**, 109410 (2021).
53. Morishige, T. et al. Effect of Al composition on the corrosion resistance of Mg-14 mass% Li system alloy. *Mater. Trans.* **57**, 1853–1856 (2016).
54. Hou, L. et al. Investigating the passivity and dissolution of a corrosion resistant Mg-33at.%Li alloy in aqueous chloride using online ICP-MS. *J. Electrochem. Soc.* **163**, C324–C329 (2016).
55. Yan, Y. M. et al. Investigating the structure of the surface film on a corrosion resistant Mg-Li(-Al-Y-Zr) alloy. *Corrosion* **75**, 80–89 (2018).
56. Yan, Y. M., Qiu, Y., Gharbi, O., Birbilis, N. & Nakashima, P. N. H. Characterisation of Li in the surface film of a corrosion resistant Mg-Li(-Al-Y-Zr) alloy. *Appl. Surf. Sci.* **494**, 1066–1071 (2019).
57. Tang, S. et al. The composition-dependent oxidation film formation in Mg-Li-Al alloys. *Corros. Sci.* **187**, 109508 (2021).
58. Argade, G. R., Panigrahi, S. K. & Mishra, R. S. Effects of grain size on the corrosion resistance of wrought magnesium alloys containing neodymium. *Corros. Sci.* **58**, 145–151 (2012).

Acknowledgements

The authors are grateful for financial support from the Australian National University (ANU) Futures Scheme, Japan New Energy and Industrial Technology Development Organization (NEDO) Innovation Structural Materials Project (Future Pioneering Projects), National Natural Science Foundation of China (Grant No. 52035005), and Swedish Research Council and the Royal Swedish Academy of Engineering Sciences. We acknowledge the use of facilities at the ANU Centre for Advanced Microscopy, Monash Centre for Electron Microscopy, Nodes of Microscopy Australia, and Monash X-ray Platform. Z.R. Zeng acknowledges the assistance of FIB and TEM from Dr. Frank Brink

and Dr. Felipe Kremer, and help with processing XPS data from Mr Chengkai Sun, and helpful discussion with Dr. Yuanming Yan.

Author contributions

Z.R.Z. designed the experiments, analyse experimental results, and draft the manuscript. M.Z.Z. produced alloy and performed FSP and mechanical testing. M.E. performed a part of corrosion tests and analysis. Y.M.Z. performed atomic resolution HAADF-STEM characterisation. S. Choudhary performed a part of corrosion tests. J.G. and Y.H. conducted XPS and data analysis. J.S.M. performed in situ XRD. Y.C. helped with TEM characterisation. A.G. helped with corrosion tests and performed profilometer characterisation. Q.Y.S. and H.F. supervised the alloy manufacturing and FSP. N.B. contributed to the experimental design, electrochemical tests and analysis, and manuscript preparation.

Competing interests

The authors declare no competing interests.

Additional information

Supplementary information The online version contains supplementary material available at <https://doi.org/10.1038/s43246-022-00245-3>.

Correspondence and requests for materials should be addressed to Zhuoran Zeng or Mengran Zhou.

Peer review information *Communications Materials* thanks Zhiming Li, Sean Agnew and the other, anonymous, reviewer for their contribution to the peer review of this work. Primary Handling Editors: Xiaoyan Li and John Plummer. Peer reviewer reports are available.

Reprints and permission information is available at <http://www.nature.com/reprints>

Publisher's note Springer Nature remains neutral with regard to jurisdictional claims in published maps and institutional affiliations.



Open Access This article is licensed under a Creative Commons Attribution 4.0 International License, which permits use, sharing, adaptation, distribution and reproduction in any medium or format, as long as you give appropriate credit to the original author(s) and the source, provide a link to the Creative Commons license, and indicate if changes were made. The images or other third party material in this article are included in the article's Creative Commons license, unless indicated otherwise in a credit line to the material. If material is not included in the article's Creative Commons license and your intended use is not permitted by statutory regulation or exceeds the permitted use, you will need to obtain permission directly from the copyright holder. To view a copy of this license, visit <http://creativecommons.org/licenses/by/4.0/>.

© The Author(s) 2022